SPECIAL FEATURE

Coherent Lagrangian swirls among submesoscale motions

F. J. Beron-Vera[a], A. Hadjighasem[b,c], Q. Xia[d], M. J. Olascoaga[e], and G. Haller[f,1]

[a]Department of Atmospheric Sciences, Rosenstiel School of Marine and Atmospheric Science, University of Miami, Miami, FL 33149; [b]Department of Mechanical Engineering, Massachusetts Institute of Technology, Cambridge, MA 02139; [c]Department of Mechanical Engineering, Amirkabir University of Technology, Tehran, District 6, Iran; [d]Institute of Oceanology, Chinese Academy of Sciences, Qingdao, 266071 Shandong, China; [e]Department of Ocean Sciences, Rosenstiel School of Marine and Atmospheric Science, University of Miami, Miami, FL 33149; and [f]Institute for Mechanical Systems, Swiss Federal Institute of Technology (ETH), 8092 Zurich, Switzerland

Edited by Snezhana I. Abarzhi, The University of Western Australia, Crawley WA, Australia, and accepted by Editorial Board Member David A. Weitz February 4, 2018 (received for review October 6, 2017)

The emergence of coherent Lagrangian swirls (CLSs) among submesoscale motions in the ocean is illustrated. This is done by applying recent nonlinear dynamics tools for Lagrangian coherence detection on a surface flow realization produced by a data-assimilative submesoscale-permitting ocean general circulation model simulation of the Gulf of Mexico. Both mesoscale and submesoscale CLSs are extracted. These extractions prove the relevance of coherent Lagrangian eddies detected in satellite-altimetry–based geostrophic flow data for the arguably more realistic ageostrophic multiscale flow.

Lagrangian coherence | mesoscale eddies | submesoscale eddies | satellite altimetry | high-resolution ocean models

APPLIED MATHEMATICS

Advances in nonlinear dynamical systems theory over the past few years (1–5) have enabled the discovery of unexpectedly resilient mesoscale material eddies in ocean velocity fields derived from satellite-sensed sea-surface height (SSH) fields (6). Ranging between 50 km and 250 km in diameter, these supercoherent Lagrangian eddies show no breakup or disintegration over a period of several months, in some cases up to 2 y (3, 7–10). Detected in a fashion fully independent from the observer, such Lagrangian eddies are bounded by uniformly stretching fluid (i.e., material) loops that stationarize the material-line–averaged tangential strain functional (3, 4). As a result, these material boundaries or elliptic Lagrangian coherent structures (11) will nearly exactly reassume their initial arc length at the end of the coherence assessment interval. Coupled with area preservation in the incompressible case, the preservation of boundary length renders these special Lagrangian eddies coherent to a previously undocumented and unexpected degree.

The presence of one such supercoherent Lagrangian eddy in the Gulf of Mexico has recently been confirmed by independent measurements of satellite-derived chlorophyll and satellite-tracked drifter paths (12). On the other hand, while satellite-based measurements are widely used for monitoring mesoscale variability in the ocean (13), they are incapable of resolving submesoscales, ranging from 100 m to a few tens of kilometers (14). There is, therefore, reason to believe (15, 16) that unresolved submesoscale motions, if sufficiently energetic, will erode the boundaries of supercoherent Lagrangian eddies inferred from satellite data. For this reason, the ubiquitous presence of submesoscale turbulence in the ocean (17, 18) has casted some doubt on the practical relevance of supercoherent mesoscale eddies inferred from satellite altimetry.

The goal of this paper is to demonstrate that, even in the presence of active submesoscale motions, mesoscale swirling structures will exist, even though their boundaries will show increased filamentation relative to the supercoherent boundaries inferred from satellite altimetry. Such material interfaces will constrain mixing in the presence of multiscale ocean motions, ranging from largely geostrophic (balanced, equilibrated) mesoscale motions to likely ageostrophic (imbalanced, unequilibrated) submesoscale motions. We reveal these coherent material entities, referred to as coherent Lagrangian swirls (CLSs) in this paper, by applying two recently developed objective (observer-independent) techniques on a surface flow generated by a submesoscale-permitting ocean circulation model. The success of these two recent techniques in framing CLSs arises from their ability to consistently locate material boundaries with a nonzero but still limited degree of filamentation. We are unaware of other available techniques that have shown a similar ability across a range of different flow conditions (cf. ref. 19, for a recent systematic comparison of available Lagrangian coherence detection methods).

The first technique detects coherence based on the Lagrangian-averaged vorticity deviation (LAVD) introduced by Haller et al. (20). Based on vorticity, this method should appear most natural to physical oceanographers, identifying CLS boundaries as a maximal set of fluid elements completing the same total material rotation relative to the mean material rotation of the whole fluid mass. This relative rotation is measured by an observer-independent angle given precisely by the LAVD along the fluid particles, as has been obtained using a recent dynamical generalization of the classic polar decomposition (cf. ref. 21). An outermost closed LAVD level curve therefore serves as the material boundary of a CLS.

The second technique used here is the spectral clustering method, first introduced by Hadjighasem et al. (22) in the context

Significance

The detection of vortices in geophysical flows is important because of their role in global circulation and transport. The recent theory of elliptic Lagrangian coherent structures has shown that long-lived, coherent material eddies exhibiting no filamentation can be extracted from altimetry-derived surface velocities associated with slow, mesoscale motions in the ocean. Since similarly perfect eddies may not be expected to exist in the presence of faster, submesoscale motions, it has remained unclear whether persistent and materially coherent eddies can in fact be identified objectively even in highly resolved ocean data. Here we show that under a suitable extension of the notion of material coherence, coherent eddies at the mesoscale and submesoscale level can indeed be simultaneously detected from multiscale velocity data.

Author contributions: F.J.B.-V., M.J.O., and G.H. designed research; F.J.B.-V., A.H., Q.X., and M.J.O. performed research; A.H. and G.H. contributed new analytic tools; and F.J.B.-V., A.H., and G.H. wrote the paper.

The authors declare no conflict of interest.

This article is a PNAS Direct Submission. S.I.A. is a guest editor invited by the Editorial Board.

[1]To whom correspondence should be addressed. Email: georgehaller@ethz.ch.

This article contains supporting information online at www.pnas.org/lookup/suppl/doi:10.1073/pnas.1701392115/-/DCSupplemental.

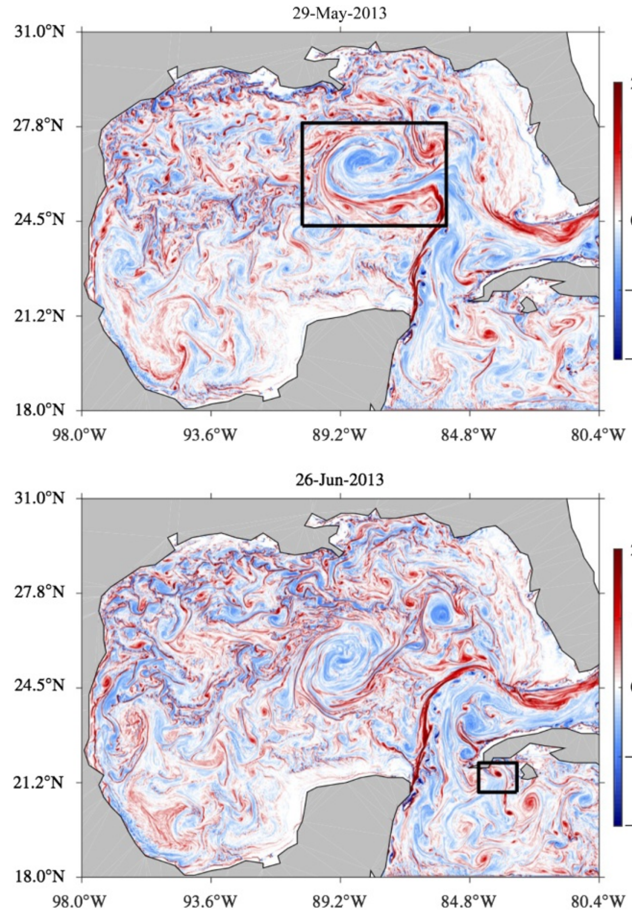

Fig. 1. Snapshots on May 29 (*Top*) and June 26 (*Bottom*), 2013, of surface ocean vorticity (normalized by the mean Coriolis parameter in the domain) produced by a data-assimilative 1-km NCOM simulation of the Gulf of Mexico.

of coherent Lagrangian vortex detection. Using graph-theoretical methods, this technique identifies CLSs as coherent fluid trajectory clusters within the total set of available fluid trajectories. A coherent cluster is defined as a material region in which particles, at all times, maintain short distances among themselves relative to their distances to particles outside the region.

The multiscale surface flow analyzed here is produced by a data-assimilative Navy Coastal Ocean Model (NCOM) of the Gulf of Mexico at 1-km horizontal resolution (23). This flow has been shown to reproduce relative dispersion statistics (24) observed during the Grand Lagrangian Experiment (GLAD) in the northern Gulf of Mexico (25), a period during which submesoscale motions were argued (26) to be active.

Results

We begin by discussing aspects of the instantaneous surface vorticity ω produced by the NCOM simulation of the Gulf of Mexico, described in *Supporting Information*, Section 2. Snapshots of the surface vorticity on May 29 and June 26, 2013, are shown in Fig. 1, normalized by the mean Coriolis parameter f in the domain. Note the abundance of eddy-like features with diameters spanning the mesoscale range (50–250 km) and the upper limb of the submesoscale range (5–25 km); for reference, the mean internal Rossby radius of deformation is about 45 km in the Gulf of Mexico (27). Also note the abundance of suprainertial ($|\omega|/f > 1$) regions interspersed among subinertial ($|\omega|/f < 1$) regions. This suggests that the surface circulation is a complex mixture of multiscale motions, ranging from predominantly slow (geostrophic) mesoscale motions, to faster (ageostrophic) marginally submesoscale motions.

Our main focus here is the mesoscale vorticity feature whose position on May 29, 2013, is indicated by a rectangle in Fig. 1, *Top*. As noted by Olascoaga et al. (12), this is the Eulerian signature of a Loop Current ring that was independently observed via satellite altimetry by the Horizon Marine Inc.'s EddyWatch program (www.horizonmarine.com). This observation used Leben's methodology (28) to search for Eulerian footprints of rings in the SSH field. Olascoaga et al. (12) classified the observed ring as Lagrangian, uncovering a theoretical mesoscale-resolved material boundary that experienced zero net stretching for 200 d from the detection date on May 29, 2013. Olascoaga et al. (12) confirmed the Lagrangian coherence of the selected material ring from satellite-derived chlorophyll data, which revealed a clear chlorophyll-deficient patch well constrained by the coherent Lagrangian boundary of the ring. The absence of material filamentation in the theoretical Lagrangian eddy boundary was further supported by satellite-tracked drifters deployed near the ring (12). These drifter tracks exhibited largely wiggle-free trajectories circling around the ring, remaining in close proximity to its altimetry-inferred coherent Lagrangian boundary.

Olascoaga et al. (12) further showed that geostrophic currents derived from the SSH field produced by the model (subsampled at mesoscale resolution) predict a mesoscale coherent Lagrangian ring similar to that detected from satellite altimetry, albeit with a shorter coherence timescale. Yet the full submesoscale surface velocity field produced no perfectly coherent Lagrangian ring, likely due to the enhanced submesoscale activity present in the simulation. Olascoaga et al. (12) nevertheless

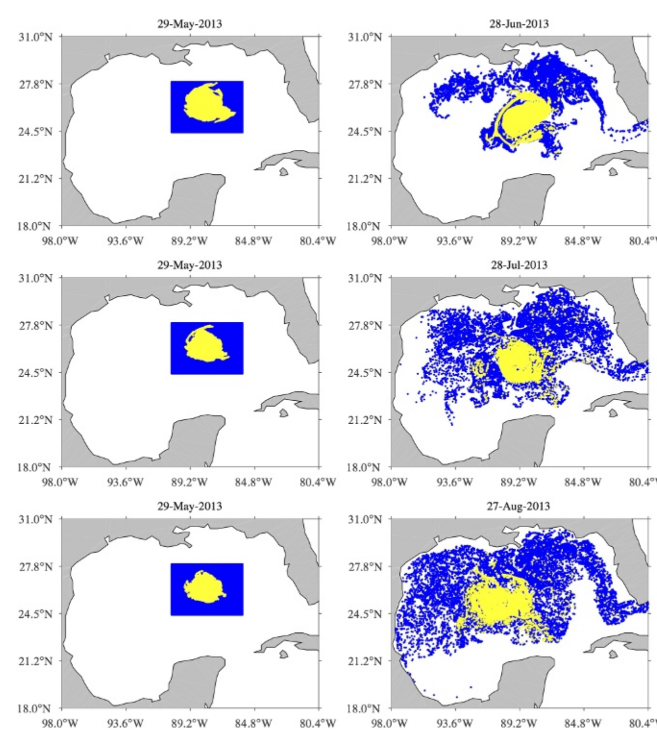

Fig. 2. Mesoscale CLS revealed by the LAVD method within the dashed rectangular domain in Fig. 1, *Top*. From *Top* to *Bottom* are Lagrangian coherence assessments based on 30-d, 60-d, and 90-d calculations. *Left* column shows the CLS on the detection date (May 29, 2013) for each calculation in yellow. *Right* column shows the end positions of tracers initially inside (yellow) and outside (blue) the CLS.

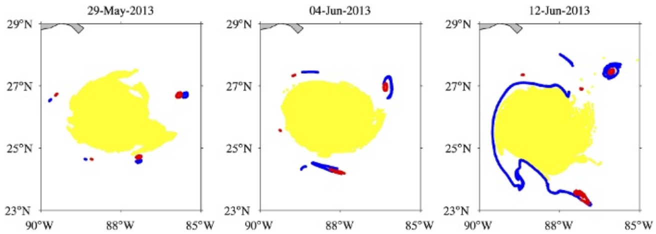

Fig. 3. Submesoscale CLSs (red) detected by the LAVD method from a 15-d calculation around the mesoscale CLS of Fig. 2 (yellow). (*Left*) The CLSs on the extraction date. (*Center* and *Right*) Snapshots of the evolution of tracers initially within these CLSs under advection. In blue are advected images of tracers within submesoscale regions initially near the extracted submesoscale CLSs.

observed that the model's surface currents produced a well-organized Lagrangian swirling structure, which we here seek to frame systematically as a mesoscale CLS.

For completeness, we also seek to reveal submesoscale CLSs. The search areas lie in the periphery of the above mesoscale vorticity feature and in the near-coastal region indicated by a rectangle in Fig. 1, *Bottom*. While we do not have observational support to justify scrutinizing these regions, the vorticity field suggests active submesoscale motions there, thereby fitting our purposes well.

LAVD Analysis. The results of various mesoscale extractions using the LAVD method (reviewed in *Supporting Information*, Section 1.2) inside the rectangular domain highlighted in Fig. 1, *Top* are shown in Fig. 2. In Fig. 2, *Top*, *Middle*, and *Bottom* rows correspond to assessments over time intervals $[t_0, t_0 + T]$, where $t_0 =$ May 29, 2013, and $T =$ 30 d, 60 d, and 90 d, respectively. Fig. 2, *Left* column shows in yellow the region occupied by the mesoscale CLS revealed by the LAVD method at time t_0. The flow-advected images of tracers initially inside and outside the CLS are shown in yellow and blue, respectively.

A first aspect to note is the topology of the boundary of the mesoscale CLS, whose area slightly decreases as the coherence horizon T is increased from 30 d to 90 d. Unlike the boundaries of coherent Lagrangian eddies revealed from satellite altimetry, the boundary of the CLS revealed from the NCOM simulation is not convex, containing smaller-scale wiggles all along it. The convexity deficiency—the area difference between a closed curve and its convex hull, normalized by the area enclosed by the closed curve—is about 0.25 for all of the coherence horizons considered.

This convexity deficiency value is too high for the LAVD method to guarantee the type of strictly tangential filamentation observed in earlier studies for altimetry-resolved mesoscale Lagrangian eddies. Indeed, such limited filamentation is observed here only partially for the 30-d extracted boundary. However, the 0.25 convexity deficiency is still low enough to prevent global breakaway of filaments, even for the 60-d and 90-d extractions periods, as seen in Fig. 2.

The lack of global breakaway of the mesoscale CLS boundaries in the three extractions is a manifestation of the distinguished property of their material elements: They all experience the same relative bulk rotation, which imparts on the boundaries a large degree of resistance to the stretching and folding induced by submesoscale motions. This is contrasted with the strong dispersion exhibited by tracers initially along the boundary of the domain of extraction (blue in Fig. 2). Even though this boundary is initially convex, the tracers it contains possess vastly different LAVD values. The corresponding vastly different total material rotation causes the materially advected image of this boundary to become fully incoherent.

Irrespective of the accuracy of this NCOM simulation relative to actual ocean currents in the same time interval, the above results show that mesoscale Lagrangian coherence continues to be present under the inclusion of active submesoscale motions.

We now further show that submesoscale CLSs coexist with their mesoscale counterparts in the same dataset. The results from 15-d and 30-d extractions in the periphery of the above mesoscale CLS centered in the Gulf of Mexico and a near-coastal domain south of Cuba in the Caribbean Sea are shown in Figs. 3 and 4, respectively. The submesoscale CLCs in the Gulf of Mexico on the extraction date (May 29, 2013) are shown in red in Fig. 3, *Left*. Also shown are the same submesoscale features but slightly displaced (in blue) and the mesoscale CLS indicated (in yellow), for reference. Two snapshots of the evolution under advection of tracers within these regions are shown in Fig. 3, *Center* and *Right*. The submesoscale CLS in the Caribbean Sea is indicated in yellow in Fig. 4, *Top*. The region outside this feature within the domain of extraction is shown in blue. The advected images of tracers initially inside these regions are shown in Fig. 4, *Bottom*. The boundaries of all extracted submesoscale CLSs have a small convexity deficiency (about 0.025). Consistent with this, the boundaries filament mostly tangentially under advection as all their elements solidly rotate in consonance. This is in stark contrast with the boundaries of the domains occupied by the slightly displaced CLSs in the Gulf of Mexico and of the domain of extraction of the CLS in the Caribbean Sea. All these domain boundaries experience vigorous stretching and folding under advection. That said, the strong Lagrangian coherence of the objectively detected submesoscale features might partially

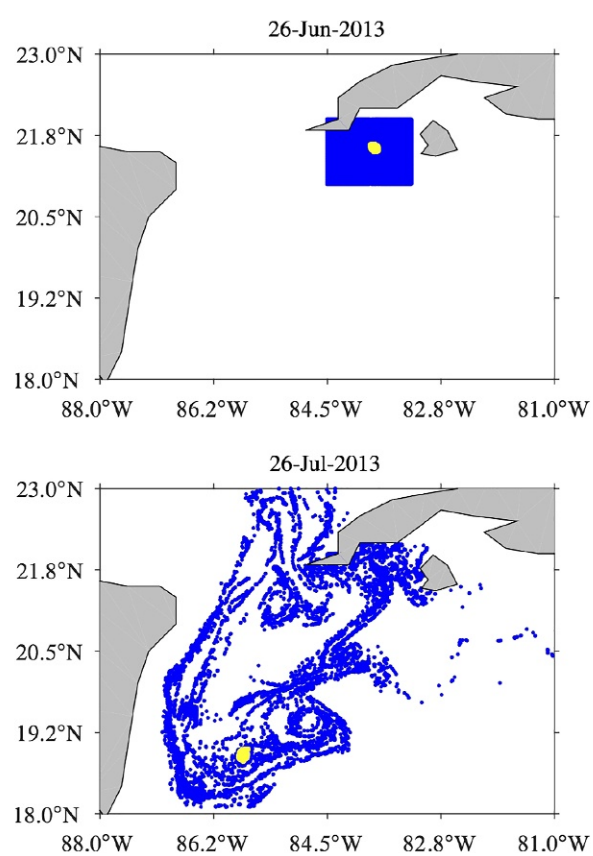

Fig. 4. A submesoscale CLS detected by the LAVD method using 30-d integration in the Caribbean Sea. (*Top*) The CLS on the detection date is shown in yellow. (*Bottom*) The end positions of tracers initially inside (yellow) and outside (blue) the CLS.

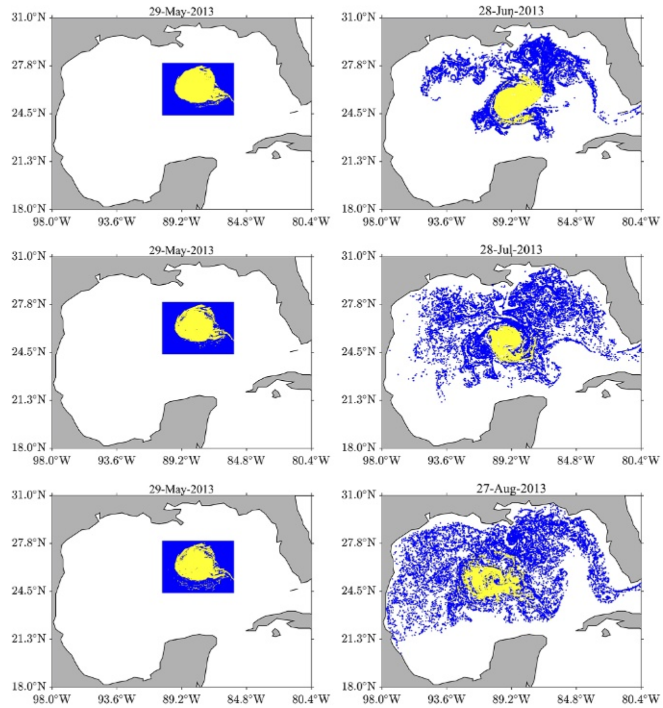

Fig. 5. As in Fig. 2, but based on the spectral clustering method.

result from the model's inability to resolve scales below those of the features.

Submesoscale CLSs of the type originating in the near-coastal domain in the Caribbean Sea can have important consequences for the effective transport of substances (such as pollutants and plankton or even larvae) from such environments into the open ocean. In turn, the submesoscale CLSs extracted in the Gulf of Mexico are offsprings of the mesoscale CLS pinched off from the Loop Current. Together, mesoscale CLSs and their satellite submesoscale CLSs contribute to transport on a larger scale.

Spectral Clustering Analysis. We now present the results from the application of the spectral clustering method (outlined in *Supporting Information*, Section 1.3), which are found to be very similar to those produced by the LAVD method. As in the previous section, for mesoscale extractions, we focus our computational effort on the rectangular domain in the center of the Gulf of Mexico. For submesoscale extractions, we focus only on the near-coastal domain in the Caribbean Sea.

In Fig. 5, *Top*, *Middle*, and *Bottom* rows show the results of mesoscale extractions for time intervals $t \in [t_0, t_0 + T]$, where t_0= May 29, 2013, and T= 30 d, 60 d, and 90 d, respectively. Fig. 5, *Left* column shows the detected mesoscale CLSs (in yellow) at the initial time t_0, and Fig. 5, *Right* column shows the advected images at the final time $t_0 + T$. As with the LAVD approach, the spectral clustering approach similarly confirms that the size of CLSs detected on t_0 = May 29, 2013, shrink as the coherence horizon T increases from 30 d to 90 d. In this computation, we have constructed the pairwise dynamic distances r_{ij} and subsequent similarity matrix W using 47,580 particles, distributed initially over a uniform grid of $244{,}195$ points. For every 30 d of integration, we have outputted the trajectory data with 100 intermediate points, evenly spaced in time. In addition, we have sparsified those edges from the complete graph representing a distance greater than $\epsilon = 200$ km.

Fig. 6, *Top* shows the submesoscale CLS south of Cuba on the extraction date t_0= June 26, 2013. Fig. 6, *Bottom* illustrates that the advected image of the CLS indeed shows limited dispersion at the final time. In this computation, we have considered a uniform grid of $270,200$ points to compute the pairwise dynamic distances r_{ij} and subsequent similarity matrix W. Additionally, we have outputted the trajectory data with 241 intermediate points and again sparsified those edges from the complete graph representing a distance greater than $\epsilon = 200$ km.

Traditional Eulerian Analysis. A natural question is whether traditional Eulerian eddy detection tools applied to the present multiscale dataset would also uncover a coherent mesoscale CLS similar to that identified by the LAVD and spectral clustering methods. Indeed, the two most broadly used eddy detection tools considered below have been argued to be capable of locating such coherent features. Their prior applications, however, invariably focused on instantaneous identification and tracking of Eulerian features without an actual verification of sustained Lagrangian coherence of the identified fluid regions.

The first Eulerian method considered here seeks regions of the flow where rotation (vorticity) dominates over deformation (strain) instantaneously. Known as the Okubo–Weiss criterion (29, 30), this method is intrinsically observer dependent and hence cannot detect material coherence in a self-consistent fashion (11). Indeed, different observers will measure different vorticities in their frames and hence will obtain different eddy boundaries using this criterion. Traditionally used in turbulence studies to detect coherent vortices (31), the method was adopted by the physical oceanography community in eddy identification from satellite altimetry (32–34). Following related work on turbulence (35), Fig. 7, *Top Left* shows (in yellow) regions where vorticity exceeds strain on May 29, 2013, by only 20% of the standard deviation of the latter. Note the varied sizes and shapes of the regions classified as coherent vortices by this criterion, which cover roughly the whole domain of extraction. Snapshots of the evolution of tracers initialized inside (yellow) and outside (blue) those regions are shown 30 d (second from *Top Left*), 60 d (third

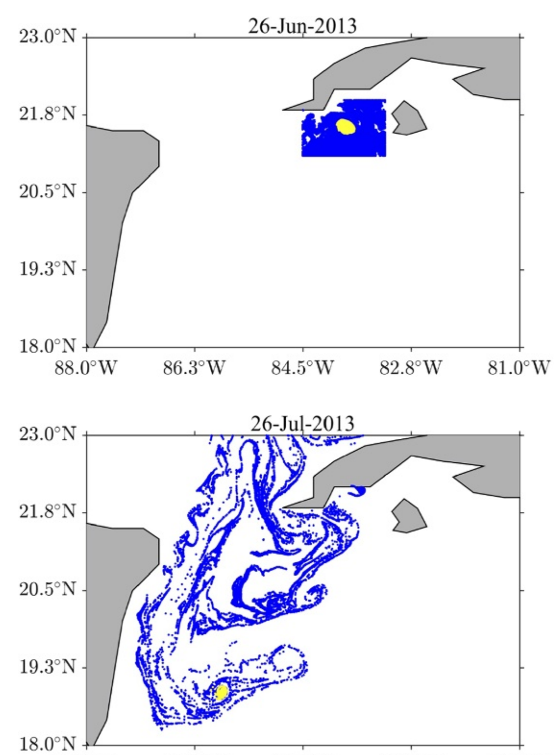

Fig. 6. As in Fig. 4, but based on the spectral clustering method.

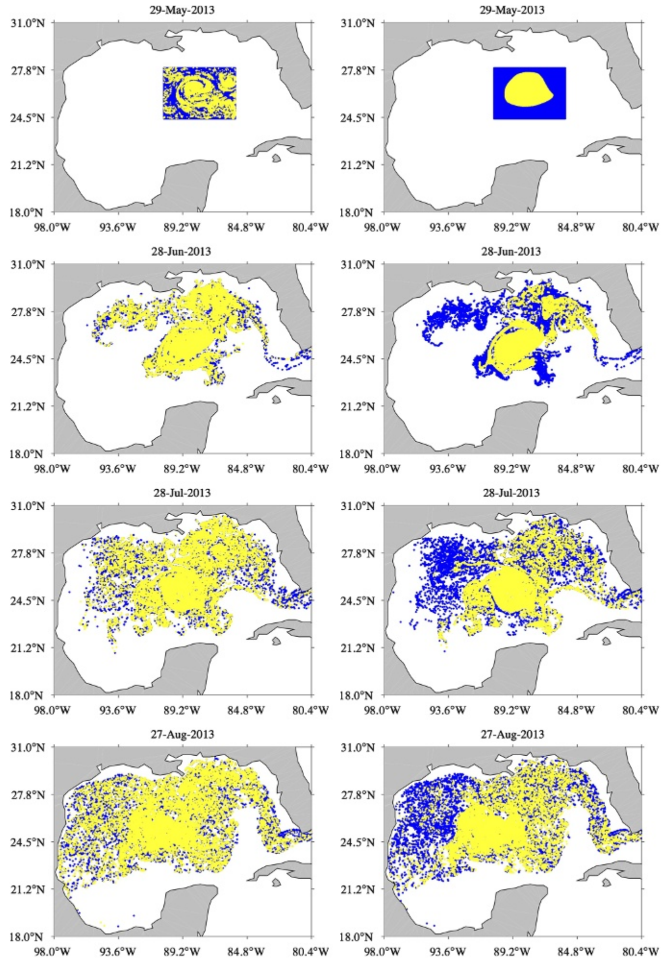

Fig. 7. Coherence assessment of the mesoscale CLS based on the Okubo–Weiss (*Left*) and SSH (*Right*) methods. *Top Left* and *Top Right* show in yellow regions where vorticity dominates over strain and which are filled with closed SSH isolines, respectively, instantaneously on May 29, 2013. From *Top* to *Bottom* each column shows snapshots of the evolution of tracers inside (yellow) and outside (blue) those regions 30 d, 60 d, and 90 d past the coherence assessment date.

from *Top Left*), and 90 d (fourth from *Top Left*) past the coherence assessment date. Also note that the dispersion experienced by the yellow tracers is just as intense as that experienced by the blue tracers. Closely accompanied by the blue tracer, significant amounts of yellow tracer are spilled over the western side of the Gulf of Mexico and also over its northeastern side before exiting through the Straits of Florida. This reveals that the Okubo–Weiss criterion fails to identify the mesoscale coherent fluid region classified as CLS by the LAVD and spectral clustering methods. One would, however, not realize this shortcoming without materially advecting the Okubo–Weiss vortical regions, as has been done here.

The second Eulerian method we consider here seeks nonlinear mesoscale eddies as regions of closed SSH isolines. An eddy is considered nonlinear if it rotates faster than it translates; i.e., the ratio U/c of the maximal mean geostrophic speed U around an eddy-interior SSH contour to the eddy translation speed c is larger than one (36). Traditionally used in oceanography to detect mesoscale eddies from satellite altimetry (37), SSH-based eddy detection has become the de facto standard for automated eddy detection and tracking (36, 38). The observer dependence of this method, too, implies an inherent inability to capture material coherence consistently (11). Nevertheless, nonlinear SSH eddies are broadly believed to carry coherent water masses (39) despite evidence to the contrary (2, 3).

Fig. 7, *Top Right* shows (in yellow) the mesoscale region occupied by a nonlinear SSH eddy on May 29, 2013. Snapshots of evolution of tracers initially inside (yellow) and outside (blue) the SSH eddy are shown in second from *Top* to *Bottom* in Fig. 7, *Right* 30 d, 60 d, and 90 d past the detection date. Note the strong dispersion experienced by a significant amount of yellow tracer despite the fact that $U/c \approx 50$ on average over 90 d for this SSH eddy. Accompanying the blue tracer, a large amount of yellow tracer is seen to exit the Gulf of Mexico through the Straits of Florida after spreading over the northeastern side of the basin. We conclude that similarly to the Okubo–Weiss criterion, the nonlinear SSH identification method also fails to capture the existing mesoscale Lagrangian coherence in this multiscale dataset.

The performance of the various methods can also be quantitatively evaluated by measuring the dispersion experienced by the fluid regions classified as coherent under advection. This is done in Fig. 8, which shows, as a function of time starting from the coherence assessment on May 29, 2013, mean pairwise distance for tracer particles filling the mesoscale fluid region classified as coherent by the LAVD (red) and spectral clustering (green) methods based on 90-d integration and the Okubo–Weiss (blue) and SSH (black) methods. Clearly, the LAVD and spectral clustering methods outperform the Okubo–Weiss and SSH methods in framing the region occupied by the mesoscale CLS by maintaining, or even increasing (in the case of spectral clustering), the compactness of the fluid region under advection.

Conclusions

We have shown that coherent mesoscale Lagrangian eddies, detected earlier only in mesoscale-resolving ocean data, continue to persist under the addition of energetic submesoscale velocity features. Specifically, in a submesoscale-permitting simulation of the Gulf of Mexico, we used two recent nonlinear dynamics methods to uncover CLSs, which are multiscale generalizations of coherent Lagrangian vortices with nonfilamenting boundaries. We have also found CLSs to coexist with a highly coherent submesoscale eddy in the same region. For the same dataset, the two most frequently used Eulerian detection methods have failed to identify features that have remained coherent over the time period of our study.

All this adds further support to the relevance of altimetry-based, mesoscale eddy detection via observer-independent and mathematically justified methods. Indeed, our present study

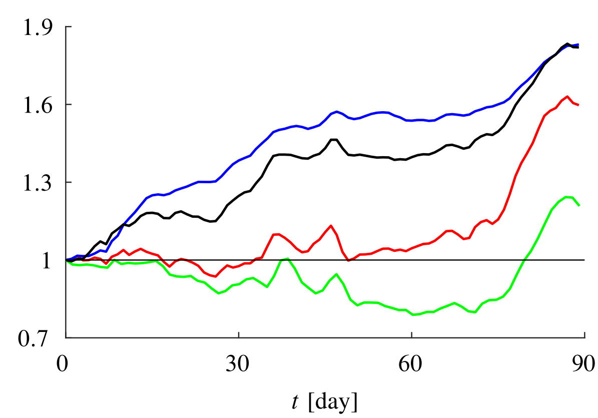

Fig. 8. Mean pairwise distance for tracer particles inside the mesoscale CLS revealed from a 90-d LAVD (red) and spectral clustering (green) calculation and for tracer particles initially within the boundary of mesoscale CLS as assessed by the Okubo–Weiss (blue) and SSH (black) methods. All four graphs are normalized by their value taken at the initial time.

suggests that the removal of submesoscale velocity contributions simply acts as a spatial filter that eliminates smaller-scale variations in material eddy boundaries without impacting their existence. As a consequence, for mesoscale mass, salinity, and heat transport, ignoring submesoscale effects does not appear to affect the true transport numbers significantly, yet brings notable conceptual and numerical simplification and enables direct reliance on satellite observations.

The CLSs we have identified are inhibitors to mixing across different scales in the ocean. Specifically, these inhibitors are minimally filamenting closed material lines that largely block the transport of ocean water attributes (such as temperature, salinity, and chlorophyll concentration) between their interiors and exteriors, providing a powerful and simplified template of key coherent structures in ocean mixing.

ACKNOWLEDGMENTS. The NCOM simulation was produced at the Naval Research Laboratory and can be obtained from dx.doi.org/10.7266/N7FQ9TJ6, dx.doi.org/10.7266/N76Q1V5G, and dx.doi.org/10.7266/N72Z13F4. Support for this work was provided by the Gulf of Mexico Research Initiative (F.J.B.-V. and M.J.O.) as part of the Consortium for Advanced Research on Transport of Hydrocarbon in the Environment, by Secretaría de Energía–Consejo Nacional de Ciencia y Tecnología Grant 201441 (to F.J.B.-V. and M.J.O.) as part of the Consorcio de Investigación del Golfo de México, and by a grant from the Turbulence Superstructures priority program (to G.H.) of the German National Science Foundation (DFG).

1. Haller G, Beron-Vera FJ (2012) Geodesic theory of transport barriers in two-dimensional flows. *Physica D* 241:1680–1702.
2. Beron-Vera FJ, Wang Y, Olascoaga MJ, Goni GJ, Haller G (2013) Objective detection of oceanic eddies and the Agulhas leakage. *J Phys Oceanogr* 43:1426–1438.
3. Haller G, Beron-Vera FJ (2013) Coherent Lagrangian vortices: The black holes of turbulence. *J Fluid Mech* 731:R4.
4. Haller G, Beron-Vera FJ (2014) Addendum to 'Coherent Lagrangian vortices: The black holes of turbulence'. *J Fluid Mech* 755:R3.
5. Haller G (2016) Climate, black holes and vorticity: How on Earth are they related?. *SIAM News* 49:1–2.
6. Traon PY, Nadal F, Ducet N (1998) An improved mapping method of multisatellite altimeter data. *J Atmos Oceanic Technol* 15:522–534.
7. Wang J, Mazloff MR, Gille ST (2014) Pathways of the Agulhas waters poleward of 2°s. *J Geophy Res* 119:4234–4250.
8. Wang Y, Olascoaga MJ, Beron-Vera FJ (2015) Coherent water transport across the South Atlantic. *Geophys Res Lett* 42:4072–4079.
9. Beron-Vera FJ, et al. (2015) Dissipative inertial transport patterns near coherent Lagrangian eddies in the ocean. *Chaos* 25:087412.
10. Romero IC, et al. (2016) Tracking the Hercules 265 marine gas well blowout in the Gulf of Mexico. *J Geophys Res* 121:706–724.
11. Haller G (2015) Lagrangian coherent structures. *Ann Rev Fluid Mech* 47:137–162.
12. Olascoaga MJ, Beron-Vera FJ, Wang Y, Triñanes J, Pérez-Brunius P (2017) On the significance of coherent Lagrangian eddies revealed from satellite altimetry. arXiv: 170406186.
13. Fu LL, Chelton DB, Le Traon P-Y, Morrow R (2010) Eddy dynamics from satellite altimetry. *Oceanography* 23:14–25.
14. Thomas L, Tandon A, Mahadevan A (2008) Submesoscale ocean processes and dynamics. *Eddy Resolving Ocean Modeling*, eds Hecht H, Hasumi H (American Geophysical Union, Washington, DC), pp 17–38.
15. Mahadevan A, Thomas LN, Tandon A (2008) Comment on "Eddy/wind interactions stimulate extraordinary mid-ocean plankton blooms". *Science* 320:448b.
16. Haza A, Özgökmen TM, Hogan PJ (2016) Impact of submesoscales on surface material distribution in a gulf of Mexico mesoscale eddy. *Ocean Model* 107:28–47.
17. McWilliams JC (2008) Fluid dynamics at the margin of rotational control. *Environ Fluid Mech* 8:441–449.
18. Klein P (2009) The oceanic vertical pump induced by mesoscale and submesoscale turbulence. *Ann Rev Mar Sci* 1:351–375.
19. Hadjighasem A, Farazmand M, Blazevski D, Froyland G, Haller G (2017) A critical comparison of Lagrangian methods for coherent structure detection. *Chaos* 27:053104.
20. Haller G, Hadjighasem A, Farazmand M, Huhn F (2016) Defining coherent vortices objectively from the vorticity. *J Fluid Mech* 795:136–173.
21. Haller G (2016) Dynamically consistent rotation and stretch tensors from a dynamic polar decomposition. *J Mech Phys Sol* 86:70–93.
22. Hadjighasem A, Karrasch D, Teramoto H, Haller G (2016) Spectral clustering approach to Lagrangian vortex detection. *Phys Rev E* 93:063107.
23. Jacobs GA, et al. (2014) Data assimilation considerations for improved ocean predictability during the Gulf of Mexico Grand Lagrangian Deployment (GLAD). *Ocean Modell* 83:98–117.
24. Beron-Vera FJ, LaCasce JH (2016) Statistics of simulated and observed pair separations in the Gulf of Mexico. *J Phys Oceanogr* 46:2183–2199.
25. Olascoaga MJ, et al. (2013) Drifter motion in the gulf of Mexico constrained by altimetric Lagrangian coherent structures. *Geophys Res Lett* 40:6171–6175.
26. Poje AC, et al. (2014) The nature of surface dispersion near the Deepwater Horizon oil spill. *Proc Natl Acad Sci USA* 111:12693–12698.
27. Chelton DB, deSzoeke RA, Schlax MG, El Naggar K, Siwertz N (1998) Geographical variability of the first baroclinic Rossby radius of deformation. *J Phys Oceanogr* 28:433–460.
28. Leben RR (2005) Altimeter-derived loop current metrics. *Circulation in the Gulf of Mexico: Observations and Models*, eds Sturges W, Lugo-Fernandez A (American Geophysical Union, Washington, DC), pp 181–201.
29. Okubo A (1970) Horizontal dispersion of flotable particles in the vicinity of velocity singularity such as convergences. *Deep Sea Res Oceanogr Abstr* 12:445–454.
30. Weiss J (1991) The dynamics of enstrophy transfer in two-dimensional hydrodynamics. *Physica D* 48:273–294.
31. Provenzale A (1999) Transport by coherent barotropic vortices. *Annu Rev Fluid Mech* 31:55–93.
32. Isern-Fontanet J, García-Ladona E, Font J (2003) Identification of marine eddies from altimetric maps. *J Atmos Oceanic Technol* 20:772–778.
33. Fang F, Morrow R (2003) Evolution, movement and decay of warm-core Leeuwin Current eddies. *Deep Sea Res Part II* 50:2245–2261.
34. Chelton DB, Schlax MG, Samelson RM, de-Szoeke RA (2007) Global observations of large oceanic eddies. *Geophys Res Lett* 34:L5606.
35. Pasquero C, Provenzale A, Babiano A (2001) Parametrization of dispersion in two-dimensional turbulence. *J Fluid Mech* 439:279–303.
36. Chelton DB, Gaube P, Schlax MG, Early JJ, Samelson RM (2011) The influence of nonlinear mesoscale eddies on near-surface oceanic chlorophyll. *Science* 334:328–332.
37. Gordon A (1986) Interocean exchange of thermocline water. *J Geophys Res* 91: 5037–5046.
38. Chelton DB, Schlax MG, Samelson RM (2011) Global observations of nonlinear mesoscale eddies. *Prog Oceanogr* 91:167–216.
39. Zhang Z, Wang W, Qiu B (2014) Oceanic mass transport by mesoscale eddies. *Science* 345:322–324.